Lithological control on topographic relief evolution in a slow tectonic setting (Anti-Atlas, Morocco)

Romano Clementucci[1,2*], Paolo Ballato[1], Lionel L. Siame[2], Claudio Faccenna[1,4], Ahmed Yaaqoub[3], Abderrahim Essaifi[3], Laëtitia Leanni[2], Valery Guillou[2]

[1] *Dipartimento di Scienze, Università Roma Tre, Largo San Leonardo Murialdo 1, 00146 Rome, Italy.*

[2] *Aix-Marseille Univ., CNRS, IRD, INRAE, Collège de France, CEREGE, Aix-en Provence, France.*

[3] *Département de Géologie, FSSM, B.P. 2390, Université Cadi Ayyad, Marrakech, Morocco.*

[4] *GFZ-German Research Centre for Geosciences, Potsdam, Germany.*

*Corresponding author: romano.clementucci@uniroma3.it

Keywords

cosmogenic nuclides, quantitative geomorphology, bedrock erodibility, denudation rates, Atlas Mountains, topographic relief

Abstract

Topographic relief results from the complex interactions between tectonics and erosional surface processes, which are primarily mediated by bedrock erodibility and climatic conditions. Ancient orogens offer a favourable setting to isolate the contribution of lithology, as tectonically driven rock uplift is typically negligible and rock strength variability can exert a critical role on the evolution of the topography. The Anti-Atlas in NW Africa is a late Paleozoic orogen comprising a well-preserved, elevated, relict landscape delimited by non-lithological knickpoints, that was uplifted during a regional late Cenozoic phase of topographic rejuvenation. Here, we combine a geomorphic analysis with ^{10}Be-derived denudation rates to quantify bedrock erodibility and get insight into the surface evolution of the Anti-Atlas and the adjacent Siroua Massif. Specifically, we show that ^{10}Be basin-wide denudation rates for the

relict landscape are rather uniform and range from 5 to 12 m/Myr. These rates agree with long-term rates estimated from different methods suggesting that the relict topography archives erosional quasi-erosional steady-state conditions at least since the latest Cretaceous. The uniformly low ^{10}Be denudation rates in the relict topography are consistent despite the variability in channel steepness and topographic relief that correlates with changes in rock type. The expansion of this analysis to the denudation rates of the downstream portion of the landscape, allows to demonstrate a linear relationship between denudation and channel steepness for catchments draining quartz bearing lithologies. This provides the chance to constrain a narrow range of bedrock erodibility values for different rock-types (quartzite, granitic and sedimentary rocks). These values are comparable with estimates from other slowly deforming settings. Specifically, our compilation from tectonically inactive to slow tectonic regions indicates that bedrock erodibility does not change significantly across different climatic zones and precipitation regimes. This highlights the critical role of lithology in controlling the production of topographic relief in post-orogenic/ slow tectonic settings. Finally, we calculate the predicted denudation rates for the steeper portions of the landscape that adjusted to the new uplift rates based on the linear correlation between erosion rates and normalized steepness indices. These rates range from 20 to 50 m/Myr and agree with the direct measurements from two catchments.

1. Introduction

Numerical modelling studies, together with qualitative and quantitative investigations have largely demonstrated the role of tectonics and climate in controlling landscape characteristics in tectonically active regions (Kirby and Whipple, 2001; Kirby and Whipple, 2012; Adams et al., 2020). Conversely, in tectonically quiescent settings, the dominant mechanisms that sustain topographic relief over longer time scales (10^6-10^8 yr) are less well understood. In these

53 regions, the relationship between topographic metrics (*i.e.*, basin-averaged slope, local relief,
54 and normalized steepness index) and erosion/rock-uplift rates suggests that climate and
55 bedrock erodibility exert a major control on landscape evolution, channel morphology, and
56 bedrock incision dynamics (Jansen et al., 2010; Scharf et al., 2013; Gallen, 2018; Peifer et al.,
57 2021). However, the quantification of bedrock erodibility is challenging since erodibility may
58 span a broad spectrum of magnitude while its physical and chemical controlling parameters
59 (i.e., degree of weathering, fracture density, rock strength) are still poorly constrained (Stock
60 and Montgomery, 1999; Kirby and Whipple, 2001; Jansen et al., 2010; Harel et al., 2016;
61 Gallen et al., 2018; Zondervan et al., 2020; Piefer et al., 2021). Importantly, in tectonically
62 inactive and slowly deforming mountain ranges some of the complications in isolating the
63 relationships between topographic relief creation and bedrock erodibility are minimized. This
64 because spatial and temporal changes in rock uplift, localized high-amplitude uplift driven by
65 faulting, and rock damage associated with seismic shaking are not dominant processes (Scharf
66 et al., 2013; Gallen et al., 2018; Peifer et al., 2021).

67 The Anti-Atlas of NW Africa is a late Palaeozoic orogen that experienced concurrent
68 surface uplift and topographic rejuvenation during the late Cenozoic most likely in response to
69 deep mantle processes (Missenard et al., 2008; Frizon de Lamotte et al., 2009; Guimera et al.,
70 2011; Miller and Becker, 2014). Although the flanks of the Anti-Atlas are steeply dissected by
71 fluvial erosion, the top of the range is characterized by a well-preserved, elevated, relict
72 landscape consisting of crystalline basement and Upper Precambrian to Paleozoic sedimentary
73 rocks. Thermochronometric data suggest that such a basement has been slowly eroding at few
74 tens of meters per million years since the latest Cretaceous (Lanari et al., 2020a; 2020b).
75 Furthermore, the Anti-Atlas has not been subjected to any extensive tectonic drift across
76 climatic zones during the Cenozoic that may have changed dramatically the erosional
77 conditions (Burkhard et al., 2006). Rather, it has experienced an overall aridification associated

78 with the establishment of the Sahara Desert since at least 2-3 Ma and possibly earlier (7-11
79 Ma) with intervening short wetter phases (Zhang et al., 2014). These characteristics offer a
80 favourable setting to study the lithological control on the short- and long-term evolution of
81 topographic relief. Specifically, this configuration rises the following research questions: what
82 are the denudation rates in the relict and in the adjusted landscapes? How do topographic
83 metrics correlate with these denudation rates? How does bedrock erodibility vary in this region
84 and other tectonically inactive settings around the world?

85 To achieve these goals, we present in situ-produced ^{10}Be-derived basin-wide denudation
86 rates and erosion rate estimates from the eroded volumes of Miocene volcanic flows emplaced
87 along paleo-valleys on the same relict surface. These rates are consistent with low-temperature
88 thermochronometric derived rates demonstrating that denudation rates have been rather
89 uniform over different time scales. Furthermore, we show that the ^{10}Be-derived denudation
90 rates from the relict landscape are uncorrelated with the topographic metrics. Conversely, the
91 ^{10}Be-derived denudation rates for the entire landscape (*i.e.*, including the steepest, adjusted
92 landscape) exhibit a strong linear correlation with the topographic metrics when catchments
93 are classified according to the quartz-bearing lithology exposed on the surface. Overall, these
94 two observations offer insights into the quantification of bedrock erodibility and its role in
95 generating topographic relief. Finally, we discuss the predicted denudation rates on the adjusted
96 topography, despite the mechanisms that drive the Cenozoic topographic rejuvenation are
97 beyond the scope of this study.

98

99 **2. Anti-Atlas and Siroua Massif**

100 The Anti-Atlas is the southern extent of the Atlas orogenic system of Morocco (North
101 Africa) (Fig. 1). Basement rocks of the region were formed during the Eburnean (early to
102 middle Paleoproterozoic) and the Pan-African (late Neoproterozoic) orogenesis, and comprise

granitic, metamorphic, and slightly metamorphosed conglomerates. These rocks are unconformably overlain by sedimentary rocks including Upper Precambrian marine carbonates, Lower Cambrian carbonates and marls, and Middle Cambrian to Middle Devonian sandstone and shales (Fig. 2a; Burkhard et al., 2006), that were deformed during the late Paleozoic, Variscan orogeny (Burkhard et al., 2006; Soulaimani et al., 2014). Currently, the Anti-Atlas forms an elongated (~ 600 km), WSW-ENE oriented topographic ridge, with a mean elevation of ~2 km, resulting from a regional late Cenozoic topographic rejuvenation, likely attributed to mantle dynamics (Sebrier et al., 2006; Frizon de Lamotte et al., 2009; Miller and Becker, 2014; Lanari et al., 2022). The elevated axial zone of the belt is characterized by an area of low-topographic relief known as the "high erosional surface" (Choubert, 1952; Missenard et al., 2008; Guimera et al., 2011). This geomorphic feature is mostly composed of Precambrian basement and Upper Precambrian to Paleozoic sedimentary rocks (Fig. 2a). A similar erosional feature has been observed in the Appalachians, the north American counterpart of the Variscan orogens in Africa and Europe (Burkhard et al., 2006; Gallen et al., 2013; Miller et al., 2013). There, the persistence of high topography is thought to be sustained by isostasy, drainage reorganization related to rock strength differences (Gallen, 2018) and/or changes in mantle dynamics (Gallen et al., 2013; Miller et al., 2013), while the relict highlands have been slowly eroding at least since the Miocene and likely much longer (Matmon et al., 2003). The central sectors of the Anti-Atlas are juxtaposed to the north to the Siroua Massif, which rises at an elevation of ~3.3 km. This range is sandwiched between the Anti-Atlas and the High-Atlas and consists of a Mio-Pliocene strato-volcano (Berrahma and Delaloye, 1989) built up over the same high erosional surface, which here is mostly sculpted on Precambrian granites (Missenard et al., 2008; Guimera et al., 2011).

3. Methods

3.1. Stream profiles, network and topographic analysis

The stream power incision model can describe the variation of channel elevation in time (*dz/dt*), as a function of upstream contributing drainage area and channel slope (Howard and Kerby, 1983; Whipple and Tucker, 1999):

$$\frac{dz}{dt} = U - KA^m S^n \quad (1)$$

where *U* is the rock uplift rate, *K* is the erodibility coefficient controlled by bedrock lithology, climate and sediment load, *A* is drainage area, *S* is local channel slope and *m* and *n* are constants, that depend on basin hydrology, channel geometry, and erosion processes (Whipple and Tucker, 1999). Under steady-state conditions, the erosion rate (*E*) and rock uplift rate (*U*) are in balance (Kirby and Whipple, 2012), and hence there are no changes in the elevation of the channel bed with time (*dz/dt* = 0). Accordingly, equation (1) can be written as:

$$S = \left(\frac{U}{K}\right)^{\frac{1}{n}} A^{-\left(\frac{m}{n}\right)} \quad (2)$$

where $(U/K)^{1/n}$ is the channel steepness index (*ks*) and *m/n* is the concavity index (θ). Equation (2) can be integrated, assuming steady state condition and spatially invariant uplift and erodibility (Perron and Royden, 2013):

$$z(x) = z(x_b) + \left(\frac{U}{KA_0^m}\right)^{\frac{1}{n}} \int_{xb}^{x} \left(\frac{A_0}{A(x)}\right)^{\frac{m}{n}} dx = z(x_b) + k_s A_0^{-\left(\frac{m}{n}\right)} \chi \quad (3)$$

$$\chi = \int_{xb}^{x} \left(\frac{A_0}{A(x)}\right)^{m/n} dx \quad (4)$$

where the integral quantity χ is the independent variable, $z(x_b)$ is the intercept, *ks* (becomes k_{sn} assuming a reference value of concavity index) is the slope, and A_0 is the reference drainage area, assumed to be 1 km^2 (Perron and Royden, 2013). Thus, we performed a detailed analysis of k_{sn} and the spatial distribution of non-lithological knickpoints to explore the possible spatial changes in rock uplift rates and erodibility. The k_{sn} and concavity indices, upstream and

150 downstream of non-lithological knickpoints, were extracted from the DEM, considering a
151 critical drainage area for the channel head initiation of 1 km^2. The non-lithological knickpoints
152 were identified using available geological maps and satellite imagery and based on their
153 distribution in the χ-elevation plot (Fig. 3a). Rivers that have experienced a similar rock uplift
154 history should have similar slopes, with knickpoints clustering around similar χ values (Perron
155 and Royden, 2013), and separating stream segments with different k_{sn} (Kirby and Whipple,
156 2012; Olivetti et al., 2016).
157 We used a Shuttle Radar Topography Mission Digital Elevation Model (SRTM DEM, pixel
158 size of 90 m) for the Anti-Atlas and the Siroua Massif to extract the drainage network. The
159 stream profiles were extracted and analyzed using MATLAB scripts TopoToolbox
160 (Schwanghart and Scherler, 2014) and the Topographic Analysis Kit (TAK; Forte and
161 Whipple, 2019). Through the TAK scripts we first evaluated the k_{sn} and θ of selected streams
162 for the upstream and downstream portions of non-lithological knickpoints. Then, we used a θ_{ref}
163 of 0.45, which is the typically used value to date, to allow the effective comparison among
164 longitudinal profiles and k_{sn} values with different drainage areas (Kirby and Whipple, 2012;
165 Miller et al. 2013; Olivetti et al., 2016). This θ_{ref} falls within the range of values of our θ
166 estimates upstream and downstream of non-lithological knickpoints, from single stream
167 profiles analysis (Supplementary Table S2). Finally, we extracted basin-averaged precipitation
168 rates as a proxy for the spatial climate variation (IMERG data; Huffman et al., 2015), slope,
169 local relief and k_{sn} for the portions of the sampled catchment that include quartz-bearing
170 lithologies, to compare them with ^{10}Be-derived denudation rate (see next section;
171 Supplementary Table S5).
172
173
174

3.2. ^{10}Be-derived denudation rates

To investigate the role of bedrock erodibility in shaping the landscape, we measured the concentration of in situ-produced cosmogenic ^{10}Be of river-borne quartz from sands samples collected in active channels of 13 catchments covering most of the western and central Anti-Atlas (Fig. 1 and Table S1). The sampled catchments drain different quartz-bearing rocks including basement (mainly granite, quartzite, and slightly metamorphosed conglomerate), Precambrian carbonate, and Cambrian-Ordovician sedimentary rocks. The denudation rates are relative to the portions of the landscape providing quartz grains, hence they were calculated excluding carbonates and classifying the rest of the catchment according to the most abundant quartz-bearing lithology exposed on the surface (see similar approaches in Safran et al., 2005 and Carretier et al., 2015 among others). Specifically, we defined three quartzite, four granite and six sedimentary dominated basins (for details see supplementary material Tables S4 and S5). Most of the sampled catchments are in disequilibrium conditions (Figs. 3a) with non-lithological knickpoints delimiting a relict landscape (Fig. 2). Samples were collected upstream and downstream of these major knickpoints. Granites and quartzites, however, are mainly exposed in the highest portions of the catchments (*i.e.*, upstream of major non-lithological knickpoints; Figs. 2a and S2), therefore, most of the measured denudation rates are only representative for the relict landscape. Sample 6, located in the Siroua Massif, represents the unique case where a wide contributing area composed of granitic basement occurs downstream the major non-lithological knickpoint, while sample 8 is from a smaller catchment of the southern Anti-Atlas flank that has already adjusted to the new uplift conditions (Figs. 1 and 2a).

Full details of the method, from the initial mineral separation to the final conversion of in situ-produced ^{10}Be to basin-wide denudation rates are provided in Appendices S1 in the Supplementary material.

3.3. Erodibility coefficient (K) and calculation of predicted denudation rates

The estimates of erodibility (K) were performed using the stream power river incision model ($K = E/k_{sn}^{n}$) for $n = 1$. For our study area, this assumption seems to describe the relationship between denudation rates and channel steepness better than a power-law function ($n = 2$; section 5.2) as already shown in other slowly deforming settings (Miller et al., 2013; Mandal et al., 2015). Specifically, K values were estimated with a forced-origin linear regression in the plot k_{sn} and denudation rates.

The estimates of K for different lithologies, allowed also to calculate the predicted denudation rates upstream (where we did not have direct measurements) and downstream of non-lithological knickpoints (*e.g.*, Adams et al., 2020). The predicted denudation rate map is calculated using the different estimates of K for sedimentary, granite and quartzite rocks), n equal 1 and the map of k_{sn} (Table S6). It should be noted that the K value of the Precambrian undifferentiated basement rocks is not well-constrained. In this case we assume the same erodibility of the sedimentary rocks. The close match of k_{sn} values between sedimentary and Precambrian undifferentiated rocks (which are mostly sedimentary and meta-sedimentary rocks) in the Anti-Atlas suggests that there is not a major variation in erodibility between these lithologies (Fig. 2). Finally, basin-averaged denudation rates and normalized channel steepness for different lithologies (mainly granitic rocks and quartzites) and erodibility values from our study area were integrated into a global compilation of regions characterized by slow tectonic activity (section 5.3).

3.4. Erosion rates from incised lava flows

The Siroua Massif comprises several late Miocene to Pliocene lava flows that were emplaced along paleo-valleys on top of the relict landscape over an area of approximately 500 km^2 at elevations ranging from ~2000 m up to ~3300 m (Figs. 2a and 4). These lava flows were subsequently incised mostly below the local channel base at the time of eruption. Consequently, they represent a key temporal and geometrical benchmark that offers the opportunity to estimate denudation rates over a Mio-Pliocene time scale (Fig. 4b; Table S3; Nereson et al., 2013; Ferrier et al., 2013). To do that, we mapped the lava flows deposited between 7 and 4 Ma exposed upstream the highest knickpoints marking the relict landscape (Berrahma and Delaloye, 1989; De Beer et al., 2000) (Fig. 4b, 4c). Subsequently, we reconstructed the paleo-topography by connecting the highest points of the remnant lava flows and subtracted it from the present-day topography to obtain the eroded rock volumes (Fig. 4b and 4c). Finally, we divided it by the relative drainage area of the associated catchment. The ratio between volume and area was further divided by the lava flow age to estimate basin-wide denudation rates (Supplementary Table S3).

4. Results

4.1. Regional topographic analysis

The Anti-Atlas is characterized by a high-standing topography rising to more than 2 km, while the volcanic edifice on top of the Siroua Massif represents the highest local topographic peak (3.3 km). The lowest k_{sn} and slope values are observed in the Souss and Draa basins and in the elevated axial zone (Figs. 2b and S1). Conversely, the highest k_{sn} and topographic slope values are in the lower topographic portions of the Anti-Atlas, on both the northern and southern flanks, and along the margins of the Siroua Massif (Figs. 2b and S1). A regionally widespread series of non-lithological knickpoints marks a sharp separation from the lowest and

highest k_{sn} and slope portions of the Anti-Atlas landscape (dashed line in Figs. 2 and S1). The non-lithological knickpoints are positioned on the slope break changes in the χ-transformed stream profiles and cluster in a relatively narrow range of χ values (Fig. 3a). The elevation of these non-lithological knickpoints range from ~ 850 to 1730 m from west to east (Table S2). The high-standing landscape upstream of these knickpoints has a mean k_{sn} of 36 ± 2.5 (σ = 12.8) $m^{0.9}$ and a θ of 0.12 ± 0.07 (σ = 0.34) , whereas the downstream portion has a mean k_{sn} of 88 ± 4.1 (σ = 20.3) $m^{0.9}$ and a θ of 0.47 ± 0.02 (σ = 0.12; Fig. 3b and Table S2). Importantly, within this elevated landscape, topographic slope, relief and k_{sn} values increase up to value higher than 80 $m^{0.9}$within areas characterized by the exposure of quartzites and conglomerates and decrease where granites outcrop, with values lower than 20 $m^{0.9}$ (Figs. 2c and S3, S4).

4.2. Denudation rates across time scales

^{10}Be basin-wide denudation rates from the relict landscape, range from 5 to 12 m/Myr. Maximum values of ~ 20 and 40 m/Myr are found downstream of non-lithological knickpoints in the Anti-Atlas and the Siroua Massif, respectively (see catchments 8 and 6, Figs. 1, 5 and 6). Importantly, the lowest rates are representative for the high-standing portion of the landscape (*i.e.*, upstream of major non-lithological knickpoints) as documented by the location of the sampled basins (Figs. 1 and 2) and the topographic metrics of the quartz contributing lithology exposed in these catchments (Table S4). Thus, these rates cannot be extended to the downstream steeper flanks. Conversely, the two highest rates are from a drainage basin with quartz-bearing lithologies exposed mostly downstream of non-lithological knickpoints, from a portion of the landscape adjusted to the new uplift conditions (catchments 6 and 8; see topographic metrics of Tables S4 and S5).

Basin-wide denudation rates obtained from eroded, 7- to 4-Myr-old volcanics exposed in the high-standing landscape of the Siroua Massif are very consistent with the ^{10}Be-derived rates

and vary from 11 to 24 m/Myr (mean value of 15.5 m/Myr, σ of 5 m/Myr; Fig. 5 and Table S3). These rates are also comparable to the longer-term erosion rates derived from low temperature thermochronology data (Fig. 5). Modelled erosion rates from apatite (U-Th)/He ages of basement rocks range from 10 to 50 m/Myr (mean value of 30 m/Myr, σ of 11 m/Myr) over a time scale of 70 Ma (Lanari et al., 2020a). Furthermore, the thermochronological dataset of Lanari et al. (2020a) includes 100- to 200-Myr-old apatite fission track ages, which suggest erosion rates of 20 to 40 m/Myr assuming a closure depth of ~ 4 km and a monotonic cooling. To a first approximation, we can conclude that our comparison across time scales suggests for the elevated landscape of the Anti-Atlas rather constant averaged denudation rates over the last 70 Myr and possibly earlier.

4.3. Basin-scale topographic analysis

Basin-wide denudation rates were plotted against the basin-averaged topographic metrics, k_{sn} and averaged annual precipitations for the main quartz-bearing lithologies exposed in the sampled catchments to assess the potential controls on denudation at basin-scale (Fig. 6). Basin-averaged k_{sn} ranges from 20 to 105 $m^{0.9}$ with maximum values in the Siroua Massif (Fig. 6a, and Table S5). Basin-averaged slopes and local relief in the sampled basins range from 4 to 14° and from 200 to 600 m, respectively (Fig. 6b and 6c; Table S5), with maximum values in the Siroua Massif. Overall, the basin-averaged k_{sn}, slope and local relief are well to poorly correlated with the basin-wide denudation rates, showing an R^2 of 0.64, 0.26 and 0.21, respectively (grey best-fit in Fig. 6a, 6b, 6c). The strongest correlation between basin-wide denudation rates and topographic metrics is found when the quartzite bearing basins are excluded, and only the granite and sedimentary dominated basins are considered. In this case, R^2 values are of 0.94, 0.62 and 0.78 for basin-averaged k_{sn}, slope and local relief, respectively, over 10 points (black best-fit in Fig. 6a, 6b, 6c).

By differentiating the erosion rates according to the dominant quartz-bearing lithology, highest k_{sn}, topographic slope and local relief values of about 60-65 $m^{0.9}$, 10-13° and 450-600 m, respectively, are observed in the quartzite bearing basins. In contrast, the lowest k_{sn}, slope and local relief values of about 20-40 $m^{0.9}$, 4-8° and 200-400 m, respectively, are found in granite bearing basins, except for basin 6 in the Siroua Massif (Figs. 6a, 6b, 6c and S4, Table S5). The metrics for the catchments dominated by Upper Precambrian and Paleozoic sedimentary rocks are similar to those observed for granite basins. Therefore, if the two samples with higher denudation rates from the adjusted landscape (~ 20 and 40 m/Myr) are excluded, the basin-wide denudation rates from the relict landscape of the Anti-Atlas are rather uniform despite the three-fold increase in k_{sn} values from granite/sedimentary to quartzite dominated catchments (see green bar in Fig. 6a). Finally, basin-wide denudation and averaged annual precipitation rates do not correlate across the sampled catchments (Fig. 6d).

5. Discussion

5.1. Erosional steady-state of the relict landscape

The regional spatial variation of k_{sn}, concavity and slope values delimit a low-topographic relief, high-standing region upstream of non-lithological knickpoints from a downstream steeper portion of the landscape (Figs. 2b, 3 and S1). The occurrence of a lower mean concavity (with significantly higher standard deviation) for the upstream portion of the landscape may appear unusual (Table S2), even if it agrees with the global compilation of Harel et al. (2016) and Seybold et al. (2021). Specifically, these studies showed that lower concavity values are typical of landscapes characterized by inactive tectonics and high aridity, like the Anti-Atlas. This landscape dichotomy, together with the elevation of non-lithological knickpoints (~ 850 to 1730; Table S2), suggests the presence of a preserved relict landscape at the maximum topography of the Anti-Atlas Mountains. Considering that there is no stratigraphic evidence of

a former, elevated base level associated with internal drainage conditions (*i.e.,* there are no unconformable Cenozoic lacustrine deposits), it is likely that such a base level fall reflects the widely documented phase of regional topographic rejuvenation (*i.e.,* surface uplift) that affected the entire Atlas system during the Cenozoic (Missenard et al., 2008; Babault et al., 2008; Frizon de Lamotte et al., 2009; Guimera et al., 2011; Miller and Becker, 2014). As an alternative, the formation of the rejuvenated landscapes may be associated with incision through rocks of different erodibility (Gallen, 2018). This process could have contributed to the local development of high relief topography like the cliffs observed at the contact between the basement and the overlying limestones. However, it does not necessary explain how the high-standing relict topography reached its current elevation (> 2000 m; Clementucci, 2022). The presence of such an elevated landscape has been attributed to the mantle dynamics as suggested by the occurrence of a non-isostatically compensated topography, widespread late Cenozoic alkaline magmatism and a shallow lithosphere-asthenosphere boundary (Frizon de Lamotte et al., 2009; Miller and Becker, 2014).

Although the deep-seated processes responsible for such an uplift are still poorly constrained and are beyond the scope of this study, the observations presented above indicate that the Anti-Atlas relict landscape represents an important geomorphic witness of the Cenozoic regional phase of topographic rejuvenation. There, ^{10}Be basin-wide denudation rates range from 5 to 12 m/Myr, above the relict landscape, and integrate timescales between 110,000 to 50,000 years, respectively. These values generally agree with long-term estimates from the eroded 7- to 4-Myr-old lava flows and thermochronometric data (Lanari et al., 2020a; Fig. 5). The persistence of spatially and temporally uniform erosion rates for the relict landscape at least since the late Cretaceous, suggests a long-term balance between rock uplift, that characterized the pre-rejuvenation condition, and erosion. This is further corroborated by the occurrence of uniform k_{sn} values, except for areas dominated by quartzite, (see next section)

and equilibrated river profiles upstream of non-lithological knickpoints (Figs. 2b, 3 and S5). These considerations suggest that the uplifted relict landscape has achieved an erosional steady-state with respect to the uplift regime prior to the topographic rejuvenation (*i.e.*, background uplift equal to denudation rates; Hack, 1960; Willet and Brandon, 2002; Scharf et al., 2013; Mandal et al., 2015). Despite the slow and protracted process of topographic lowering documented by the low denudation rates, rivers in the relict landscape are characterized by detachment-limited erosional conditions (Baldwin et al., 2003), where sediment transport capacity appears to be greater than the sediment supply, as observed in other post-orogenic topography and slow tectonic settings (Fig. 7b; Scharf et al., 2013; Mandal et al., 2015; Piefer et al., 2021).

5.2. Lithological control on topography

The decline of tectonic activity and consequently of rock uplift rates is thought to generate a topographic relief that is mostly controlled by lithological and climatic variations (Jansen et al., 2010; Scharf et al., 2013; Gallen et al., 2018). The impact of climate on erosional processes is addressed in section 5.4. In this section, we discuss the relationships between denudation rates, topographic relief and lithology. Specifically, our basin-wide denudation rates classified according to the dominant quartz-bearing lithology exposed in the sampled catchments show systematic patterns when compared with the topographic metrics (Fig. 6a, 6b, 6c). Thus, we observe two major patterns that bring us to two different conclusions.

The first point is that local variations in k_{sn} values for catchments with spatially and temporally constant denudation rates reflect the non-uniform rock strength distribution of the slowly eroding relict landscape of the Anti-Atlas (Jansen et al., 2010; Peifer et al., 2021). Despite the uniform erosion rates, the less erodible quartzite dominated catchments present higher topographic metrics than catchments dominated by sedimentary and the metamorphic

375 rocks (Fig. 6a, 6b, 6c). Overall, these data indicate that channel steepness and hillslope adjust
376 to compensate for rock erodibility as expected for erosional steady-state conditions (Hack,
377 1960; Jansen et al., 2010; Peifer et al., 2021). This applies also at the global scale as
378 demonstrated by the compilation showing in figure 7a, although data are not lithologically
379 differentiated. Specifically, for slow tectonic settings, the rather low correlation between basin-
380 wide denudation rates and basin averaged slope may reflect variations in erodibility or the
381 decoupling between hillslope and river incision processes (Olivetti et al., 2016; Peifer et al.,
382 2021). These findings suggest that the passive exhumation of lithologies with variable rock
383 strength plays a dominant role in producing topographic relief, despite the lack of tectonic
384 activity. Therefore, even if the relict landscape is in erosional steady-state, the topographic
385 form changes because the continuous exhumation of rocks with different erodibility critically
386 influences the process of surface lowering leading to the development of localized topographic
387 relief (*e.g.,* Piefer et al., 2020).

388 Secondly, for the Anti-Atlas, if we extend the analysis to the downstream portion of the
389 landscape the linear correlation between k_{sn} values and our denudation rates suggests that the
390 n parameter of the stream power-law (equation 1), can be approximated to 1 (Fig. 6a), despite
391 the narrow range of the dataset. Although this appears as be inconsistent with the expected
392 power-law function, it should be noted that $n > 1$ has been only observed in regions with high
393 denudation rates, and consequently steep topography, where the threshold of erosion combined
394 with a stochastic flood distribution, predict non-linearity in the k_{sn}-denudation rates
395 relationships (Ouimet et al., 2009; DiBiase and Whipple, 2011; Kirby and Whipple, 2012;
396 Harel et al., 2016; Adams et al., 2020). Thus, for a low range of denudation rates and channel
397 steepness, the linear and the power-law relationships are practically indistinguishable (Ouimet
398 et al., 2009; Scharf et al., 2013; Mandal et al., 2015; Olivetti et al., 2016). This is the case for
399 slow tectonic settings as documented by our data from the Ant-Atlas landscape (see figure 7a

where slope is lower than ca. 20° and 7b where channel steepness is lower than 200 $m^{0.9}$). In these settings, the linear fit (n = 1) better explains the observed variability in denudation rates and channel steepness respect to the power-law fit (n = 2; Figs. 7b and S8, see R^2 coefficients in Tables S6 and S7). These observations suggest that the approximation of n = 1 could allow one to effectively constrain bedrock erodibilities in the slow tectonic settings, like the Anti-Atlas Mountains.

5.3. Quantification of the bedrock erodibility parameter (*K*)

The approximation of the stream power river incision model to a linear equation offers the possibility to easily quantify the bedrock erodibility parameter (K). Specifically, our estimates of K values are 1.4 ± 0.9 x 10^{-7}, 2.2 ± 0.3 x 10^{-7} and 3.8 ± 0.4 x 10^{-7} $m^{0.1}$/ yr for quartzite, sedimentary and granitic dominated basins, respectively (Fig. 7b and Table S6). This is consistent with estimates from the Appalachians and other slow tectonic regions (SE Brazil, Cape Mountains, Peninsular Indian, Massif Central; Fig. 7b) where similar lithologies occur (Scharf et al., 2013; Mandal et al., 2015; Olivetti et al., 2016; Gallen, 2018; Peifer et al., 2021). In granite dominated catchments from different stable regions and with variable climate conditions, erodibility values are distributed in a narrow range mainly between 10^{-7} and 10^{-6} $m^{0.1}$/yr (3.8 ± 0.4 x 10^{-7} $m^{0.1}$/ yr in the Anti-Atlas relict landscape; 5.8 ± 0.1 x 10^{-7} $m^{0.1}$/ yr in the India, Mandal et al. (2015); 8.8 ± 1.9 x 10^{-7} $m^{0.1}$/ yr in south-eastern Brazil, Peifer et al. (2021); 9.2 ± 0.5 x 10^{-7} $m^{0.1}$/ yr in the Massif Central, Olivetti et al. (2016); ~5 x 10^{-7} $m^{0.1}$/ yr in the Appalachians, Gallen et al. (2018); Fig. 7b and Table S6). Conversely, in quartzite dominated catchments, K values range usually from 10^{-7} to 10^{-8} $m^{0.1}$/ yr (1.4 ± 0.9 x 10^{-7} $m^{0.1}$/ yr in the Anti-Atlas; 0.3 ± 0.04 x 10^{-7} $m^{0.1}$/ yr for the Cape Mountains; 0.2 ± 0.05 x 10^{-7} $m^{0.1}$/ yr in south-eastern Brazil; Fig. 7b and Table S6). Except for Brazil, the R^2 correlation coefficients are generally good (mostly higher than 0.82; Table S6). Indeed, the presence of

425 physically robust and chemically inert quartzite in the sampled catchments strongly decreases
426 the catchment-averaged value of K in the study area (Fig. 6a).

427 Overall, the erodibility values from tectonically inactive regions vary between 10^{-8} and 10^{-6} $m^{0.1}$/yr and are generally lower than those estimated in tectonically active orogens, where K usually ranges between 10^{-6} and 10^{-3} $m^{0.1}$/ yr (Stock and Montgomery, 1999; Kirby and Whipple, 2001; Peifer et al., 2021). There, tectonic deformation leads to the creation of fractures resulting in a general increase in bedrock erodibility (Molnar et al., 2007; Portenga and Bierman, 2011). However, quantifying the erodibility may be more complex, for example, estimates of the mechanical rock strength erodibility derived from measure of the uniaxial compressive strength (UCS; Schmidt hammer) and channel steepness in the High Atlas, indicate that granitoid rocks from the basement are more resistant than the Upper Precambrian and Paleozoic sedimentary cover (Zondervan et al., 2020). These results are clearly in contrast with our findings. However, it should be considered that the Schmidt hammer only measures small-scale intact rock strength and that other larger-scale factors (such as fracture density and degree of weathering) might be strength limiting for estimating bedrock erodibility. Thus, one might not expect a correlation between these erodibility estimates from the stream power model and the Schmidt hammer rebound values. Moreover, the High Atlas is an active mountain belt with high rates of rock uplift and exhumation (mostly > 100 m/Myr; Lanari et al., 2020a); there the granitoids are exposed in the axial zone where topographic relief is high and k_{sn} values range from 90 to 200 $m^{0.9}$ (Zondervan et al., 2020). Conversely, in the inactive Anti-Atlas, exhumation and denudation rates from the relict topography are two of order of magnitudes lower while the associated granitic rocks have a lower topographic relief (k_{sn} values range from 20 to 40 $m^{0.9}$, Fig. 6a). This means that, in the Anti-Atlas, the exposure time to physical and chemical weathering processes would be much higher than in the High Atlas. Although the relationships between denudation, topographic relief, and weathering mechanisms are difficult

to determine (von Blanckenburg, 2005), the granitic rocks exposed in the relict portion of the Anti-Atlas are most likely more weathered. This could explain while they present higher erodibility values with respect to the granites of the High Atlas.

5.4 Possible impact of climate on *K* values

The possible role of climate in modulating erosion rates can be evaluated by quantifying the occurrence of large floods that can mobilize sediments overcoming substrate detachment thresholds (Snyder et al., 2003; DiBiase and Whipple, 2011). Specifically, data from the San Gabriel Mountains of California suggest the occurrence of a peak in erosional efficiency when the mean runoff and the discharge variability increase (DiBiase and Whipple, 2011). This appears to be especially valid in regions with low topographic slope and in dry regions where runoff is lower than 500-400 mm/yr (DiBiase and Whipple, 2011). Thus, in arid settings such as the Anti-Atlas the discharge variability can represent a key issue in controlling the erosional and transport dynamics. Unfortunately, these kinds of data are often unavailable and hence to a first approximation the mean annual precipitation has been considered as a proxy for climate (Harel et al., 2016; Adams et al., 2020).

Here, we explore the climatic sensitivity on erodibility, by selecting catchments from tectonically inactive to slowly deforming regions characterized by similar rock composition that span different climatic zones. Our compilation shows erodibility estimates from granite-dominated catchments in India, where the mean annual precipitation is ~ 5000 mm/yr, that are similar to those of the Massif Central and SE Brazil (~ 1700 mm/yr), and the Anti-Atlas (~ 200 mm/yr; Supplementary Fig. S7). The same erodibility is estimated from the south-eastern Australia Escarpment and the Appalachians, which are in temperate settings and have precipitation rates ranging from 1000 to up to 2000 mm (Fig. 7b). Similarly, the erodibility estimates of quartzite-dominated catchments in SE Brazil, Cape Mountains and the Anti-Atlas

are quite similar despite the up to eightfold increase in mean annual precipitation (Fig. 7b). These observations suggest that the climatic conditions do not have a major impact on erodibility (Fig. 7b). Overall, this compilation indicates that in tectonically inactive to slowly deforming settings, climate might not play a major role on the long-term evolution of topographic relief, channel steepness and on the denudation rates at the integration timescale of ^{10}Be cosmogenic nuclides.

5.5 Predicted denudation of adjusted topography

^{10}Be-derived denudation rates were determined mostly for the relict portions of the Anti-Atlas landscape. There, the spatial variation of channel steepness reflects the different erodibility of the major rock types (granitic, sedimentary and quartzite rocks). Conversely, downstream of non-lithological knickpoints, in the landscape adjusted to the new uplift rates associated with the topographic rejuvenation, the exposed lithologies consist of Paleozoic carbonates and siliciclastic sedimentary rocks (Fig. 2a). Therefore, the denudation rates for the adjusted topography are not well-constrained because quartz-bearing-lithologies are not outcropping (except for catchments 6 and 8). Importantly, the rejuvenated portions of the landscape are characterized by a rather uniform lithology (mainly sedimentary), overcoming the common problem of the susceptibility of channel steepness to spatial variations in lithologies and/or precipitations (Scharf et al., 2013; Mandal et al., 2015; Adams et al., 2020).

The inferred rates range from 20 to 50 m/Myr (Fig. 8) in agreement with our basin-wide ^{10}Be rates from a catchment of the western Siroua Massif and the southern Anti-Atlas flank (catchment 6 and 8, respectively), which are mostly or entirely downstream of the relict landscape (Fig. 2). The relative uniformity of the predicted denudation rates map in the adjusted landscape reflects the occurrence of similar k_{sn} values at least where the lithology is uniform (Figs. 2b and 3a).

Importantly, our predicted values can be directly interpreted as modern rock uplift rates induced by the late Cenozoic topographic rejuvenation. Previous studies proposed the occurrence of a recent phase of uplift based on geophysical and structural data without direct or indirect rate estimates (Missenard et al., 2008; Frizon de Lamotte et al., 2009; Miller and Becker, 2014). This analysis allows to decipher the spatio-temporal changes in uplift during the late Cenozoic, providing a direct estimates of denudation (and rock uplift) rates along the fluvial landscapes.

6 Conclusions

Our analysis indicates that Anti-Atlas underwent a late Cenozoic rejuvenation as documented by the transient state of the stream networks. The persistence of an uplifted, relict landscape upstream of non-lithological knickpoints documents the pre-uplift erosional conditions. This uplifted topography is characterized by low value of channel steepness and denudation as typically observed in tectonically inactive or slowly deforming regions. The close agreement between short- (^{10}Be) and long-term (eroded volume of volcanic rocks and low-temperature thermochronology data) erosion rates supports the idea of erosional steady-state conditions for the relict landscape. There, catchments formed by less erodible quartzite present higher topographic metrics than basins dominated by granite and sedimentary rocks, despite the uniform ^{10}Be erosion rates ranging from 5 to 12 m/Myr. Importantly our data from the relict landscape indicate that channel steepness and hillslope adjust to compensate for rock erodibility as expected for erosional steady-state conditions. This indicates that lithology plays a major role in creating topographic relief in the slow tectonic settings.

However, if we consider our ^{10}Be-dervied denudation rates representative of the adjusted landscape downstream of non-lithological knickpoints, we observe a linear correlation between k_{sn} values and basin-wide denudation rates according to the dominant lithology exposed in the

525 catchment. This correlation allows estimation of a range of bedrock erodibility for the different
526 quartz-bearing lithologies (quartzite, granite and sedimentary rocks). When we combined our
527 results with similar data from tectonically inactive and slowly deforming regions we found a
528 similar range of erodibility values for quartzite and granite, despite a great variability in mean
529 annual precipitation rates. This suggests that climate does not appear to have a major impact
530 on the erodibility values.

531 Finally, our erodibility estimates for different lithologies allow to predict denudation rates
532 of 20 to 50 m/Myr in the downstream portions of the landscape. To a first approximation, these
533 values can be interpreted as the values of rock uplift rates associated with the late Cenozoic
534 topographic rejuvenation (independently from the causes of uplift). In conclusion, the Anti-
535 Atlas allows isolating and quantifying the impact of bedrock erodibility in shaping the
536 landscape and creating topographic relief.

537

538 **Acknowledgments**

539 This study is part of the PhD thesis of RC at the University of Roma Tre (PhD Cycle
540 XXXIV). It was supported by the PhD School of Roma Tre and grant "Vinci 2020" awarded
541 to RC (Number : C2- 1403). PB was supported by the MIUR (Ministry of Education University
542 and Research), Excellence Department Initiative, Art. 1, com. 314-337, Low 232/2016. The
543 ASTER (CEREGE, Aix-en-Provence) AMS national facility, is supported by the INSU/CNRS,
544 the ANR (Projets thématiques d'excellence programme for the Equipements d'Excellence) and
545 the IRD. We thank G. Aumaître and K. Keddadouche for their support in AMS measurements,
546 R. Lanari, S. Racano, N. Youbi and R. Braucher for stimulating discussions. We are indebted
547 to P-H Blard, S. Willett and T. Schildgen for revising this manuscript as a chapter of the PhD
548 Thesis of the first author, to S. Gallen and an anonymous Reviewer for the excellent and
549 detailed revisions, to the Editor J.P. Avouac for managing the submission of the manuscript,

and finally to L. Benedetti, M. Della Seta, P. Molin and O. Bellier for providing valuable comments during the PhD defense of RC.

References

Adams, B. A., Whipple, K. X., Forte, A. M., Heimsath, A. M., Hodges, K. V., 2020. Climate controls on erosion in tectonically active landscapes. Sci. adv. *6*(42), eaaz3166. https://www.science.org/doi/10.1126/sciadv.aaz3166.

Babault, J., Teixell, A., Arboleya, M. L., Charroud, M., 2008. A Late Cenozoic age for long-wavelength surface uplift of the Atlas Mountains of Morocco. Terra nova. *20*(2), 102-107. https://doi.org/10.1111/j.1365-3121.2008.00794.x

Baldwin, J. A., Whipple, K. X., Tucker, G. E., 2003. Implications of the shear stress river incision model for the timescale of postorogenic decay of topography. J. Geophys. Res. Solid Earth. 108(B3). https://doi.org/10.1029/2001JB000550.

Berrahma, M., Delaloye, M., 1989. Données géochronologiques nouvelles sur le massif volcanique du Siroua (Anti-Atlas, Maroc). J. Afr. Earth. Sci. 9(3-4), 651-656. https://doi.org/10.1016/0899-5362(89)90049-3.

Burkhard, M., Caritg, S., Helg, U., Robert-Charrue, C., Soulaimani, A., 2006. Tectonics of the Anti-Atlas of Morocco. C.R. Geosci. 338(1-2), 11-24. https://doi.org/10.1016/j.crte.2005.11.012.

Carretier, S., Regard, V., Vassallo, R., Martinod, J., Christophoul, F., Gayer, E., Audin L., Lagane, C., 2015. A note on ^{10}Be-derived mean erosion rates in catchments with heterogeneous lithology: Examples from the western Central Andes. Earth Surf. Processes Landforms. 40(13), 1719-1729. https://doi.org/10.1002/esp.3748.

Choubert, G., 1952. Histoire géologique du domaine de l'Anti-Atlas: Notes Mém. Serv. Géol. Maroc. 100, 77-194.

Clementucci, R., 2022. Deciphering mantle contribution on surface uplift in the Atlas-Meseta system (Morocco) (Doctoral dissertation). Earth Sciences. Università degli studi Roma Tre; Aix Marseille Univ. https://tel.archives-ouvertes.fr/tel-03630297/document.

De Beer, C. H., Chevallier, L. P., De Kock, G. S., Gresse, P. G., Thomas, R. J., 2000. Mémoire explicatif de la carte géologique du Maroc au 1/50 000, Feuille Sirwa. Notes Mem. Serv. Geol. Maroc. 395, 86.

DiBiase, R.A., Whipple, K.X., 2011. The influence of erosion thresholds and runoff variability on the relationships among topography, climate, and erosion rate. J.Geophys. Res. 116 (F4). http://dx.doi.org/10.1029/2011JF002095.

Ferrier, K. L., Perron, J. T., Mukhopadhyay, S., Rosener, M., Stock, J. D., Huppert, K. L., Slosberg, M., 2013. Covariation of climate and long-term erosion rates across a steep rainfall gradient on the Hawaiian island of Kaua 'i. Bulletin. 125(7-8), 1146-1163. https://doi.org/10.1130/B30726.1.

Frizon de Lamotte, D., Leturmy, P., Missenard, Y., Khomsi, S., Ruiz, G., Saddiqi, O., Guillocheau F., Michard A., 2009. Mesozoic and Cenozoic vertical movements in the Atlas system (Algeria, Morocco, Tunisia). An overview: Tectonophysics. 475, 9–28. https://doi.org/10.1016/j.tecto.2008.10.024.

Forte, A.M., Whipple, K.X., 2019. Short communication: the Topographic Analysis Kit (TAK) for TopoToolbox. Earth Surf. Dyn.7, 87–95. https://doi.org/10.5194/esurf-7-87-2019.

Gallen, S. F., Wegmann, K. W., Bohnenstiehl, D. R., 2013. Miocene rejuvenation of topographic relief in the southern Appalachians. GSA Today. 23(2), 4-10. https://doi.org/10.1130/GSATG163A.1.

Gallen, S. F., 2018. Lithologic controls on landscape dynamics and aquatic species evolution in post-orogenic mountains. Earth and Planet. Sci. Lett. 493, 150-160. https://doi.org/10.1016/j.epsl.2018.04.029.

Godard, V., Dosseto, A., Fleury, J., Bellier, O., Siame, L., ASTER Team., 2019. Transient landscape dynamics across the Southeastern Australian Escarpment. Earth and Planet. Sci. Lett. 506, 397-406. https://doi.org/10.1016/j.epsl.2018.11.017

Guimerà, J., Arboleya, M. L., Teixell, A., 2011. Structural control on present-day topography of a basement massif: the Central and Eastern Anti-Atlas (Morocco). Geologica Acta. 9(1), 55-65. https://doi.org/10.1344/105.00 0001643.

Hack, J. T., 1960. Interpretation of erosional topography in humid temperate regions. Am. J. Sci.258-A, 80–97. Bradley Volume.

Harel, M. A., Mudd, S. M., Attal, M., 2016. Global analysis of the stream power law parameters based on worldwide ^{10}Be denudation rates. Geomorphology. 268, 184-196. https://doi.org/10.1016/j.geomorph.2016.05.035.

Hollard, H., Choubert, G., Bronner, G., Marchand, J., Sougy, J., 1985. Carte géologique du Maroc, scale 1: 1,000,000. Serv. Carte géol. Maroc. 260(2).

Howard, A.D., Kerby, G., 1983. Channel changes in badlands. Geol. Soc. Am. Bull.94, 739–752. http://dx.doi.org/10.1130/0016-7606(1983)94<739:CCIB>2.0.CO;2.

Huffman, G. J., Bolvin, D. T., Braithwaite, D., Hsu, K., Joyce, R., Xie, P., & Yoo, S. H., 2015. NASA global precipitation measurement (GPM) integrated multi-satellite retrievals for GPM (IMERG). Algorithm Theoretical Basis Document (ATBD) Version, 4, 26. [Available online at http://pmm.nasa.gov/sites/default/files/document_files/IMERG_ATBD_V4.5.pdf.]

623 Jansen, J. D., Codilean, A. T., Bishop, P., Hoey, T. B., 2010. Scale dependence of lithological
624 control on topography: Bedrock channel geometry and catchment morphometry in
625 western Scotland. J. Geol. 118(3), 223-246. https://doi.org/10.1086/651273.
626 Kirby, E., Whipple, K. X., 2001. Quantifying differential rock-uplift rates via stream profile
627 analysis. Geology. 29(5), 415-418. https://doi.org/10.1130/0091-
628 7613(2001)029<0415:QDRURV>2.0.CO;2.
629 Kirby, E., Whipple, K. X., 2012. Expression of active tectonics in erosional landscapes. J.
630 Struct. Geol. 44, 54-75. https://doi.org/10.1016/j.jsg.2012.07.009.
631 Lanari, R., Fellin, M. V., Faccenna, C., Balestrieri, M. L., Pazzaglia, F. J., Youbi, N., Maden,
632 C., 2020a. Exhumation and surface evolution of the western high atlas and
633 surrounding regions as constrained by low-temperature thermochronology.
634 Tectonics. 39(3), e2019TC005562. https://doi.org/10.1029/2019TC005562
635 Lanari, R., Faccenna, C., Fellin, M. G., Essaifi, A., Nahid, A., Medina, F., Youbi, N., 2020b.
636 Tectonic evolution of the western high Atlas of Morocco: oblique convergence,
637 reactivation, and transpression. *Tectonics*. *39*(3), e2019TC005563.
638 https://doi.org/10.1029/2019TC005563.
639 Lanari, R., Reitano, R., Giachetta, E., Pazzaglia, F. J., Clementucci, R., Faccenna, C., Fellin,
640 M. G., 2022. Is the Anti-Atlas of Morocco still uplifting?. J. Afr. Earth. Sci. 188,
641 104481. https://doi.org/10.1016/j.jafrearsci.2022.104481.
642 Mandal, S. K., Lupker, M., Burg, J. P., Valla, P. G., Haghipour, N., Christl, M., 2015. Spatial
643 variability of ^{10}Be-derived erosion rates across the southern Peninsular Indian
644 escarpment: A key to landscape evolution across passive margins. Earth and Planet.
645 Sci. Lett. 425, 154-167. https://doi.org/10.1016/j.epsl.2015.05.050.
646 Matmon, A., Bierman, P. R., Larsen, J., Southworth, S., Pavich, M., Caffee, M., 2003.
647 Temporally and spatially uniform rates of erosion in the southern Appalachian Great

Smoky Mountains. Geology. 31(2), 155-158. https://doi.org/10.1130/0091-7613(2003)031<0155:TASURO>2.0.CO;2.

Miller, S. R., Sak, P. B., Kirby, E., Bierman, P. R., 2013. Neogene rejuvenation of central Appalachian topography: Evidence for differential rock uplift from stream profiles and erosion rates. Earth and Planet. Sci. Lett. 369, 1-12. https://doi.org/10.1016/j.epsl.2013.04.007.

Miller, M. S., Becker, T. W., 2014. Reactivated lithospheric-scale discontinuities localize dynamic uplift of the Moroccan Atlas Mountains. Geology. 42(1), 35-38. https://doi.org/10.1130/G34959.1.

Missenard, Y., Saddiqi, O., Barbarand, J., Leturmy, P., Ruiz, G., El Haimer, F. Z., Frizon de Lamotte, D., 2008. Cenozoic denudation in the Marrakech High Atlas, Morocco: insight from apatite fission-track thermochronology. Terra Nova. 20(3), 221-228. https://doi.org/10.1111/j.1365-3121.2008.00810.x.

Molnar, P., Anderson, R.S., Anderson, S., 2007. Tectonics, fracturing of rock, and erosion. J. Geophys. Res. v. 112, F03014. https://doi.org/10.1029/2005JF000433.

Nereson, A., Stroud, J., Karlstrom, K., Heizler, M., McIntosh, W., 2013. Dynamic topography of the western Great Plains: Geomorphic and $^{40}Ar/^{39}Ar$ evidence for mantle-driven uplift associated with the Jemez lineament of NE New Mexico and SE Colorado. Geosphere. 9(3), 521-545. https://doi.org/10.1130/GES00837.1.

Olivetti, V., Godard, V., Bellier, O., ASTER team., 2016. Cenozoic rejuvenation events of Massif Central topography (France): Insights from cosmogenic denudation rates and river profiles. Earth and Planet. Sci. Lett. 444, 179-191. https://doi.org/10.1016/j.epsl.2016.03.049.

671 Ouimet, W.B., Whipple, K.X., Granger, D.E., 2009. Beyond threshold hillslopes: chan-nel
672 adjustment to base-level fall in tectonically active mountain ranges. Geology. 37, 579–
673 582. http://dx.doi.org/10.1130/G30013A.1.
674 Peifer, D., Persano, C., Hurst, M. D., Bishop, P., Fabel, D., 2021. Growing topography due to
675 contrasting rock types in a tectonically dead landscape. Earth Surf. Dyn. 9(2), 167-
676 181. https://doi.org/10.5194/esurf-9-167-2021.
677 Perron, J.T., Royden, L., 2013. An integral approach to bedrock river profile analysis. Earth
678 Surf. Process. Landf. 38, 570–576. https://doi.org/10.1002/esp.3302.
679 Portenga, E. W., Bierman, P. R., 2011. Understanding Earth's eroding surface with ^{10}Be.
680 GSA today. 21(8), 4-10. http://dx.doi.org/10.1130/G111A.1.
681 Safran, E. B., Bierman, P. R., Aalto, R., Dunne, T., Whipple, K. X., Caffee, M., 2005.
682 Erosion rates driven by channel network incision in the Bolivian Andes. Earth Surf.
683 Processes Landforms. 30(8), 1007-1024. https://doi.org/10.1002/esp.1259.
684 Scharf, T. E., Codilean, A. T., De Wit, M., Jansen, J. D., Kubik, P. W., 2013. Strong rocks
685 sustain ancient postorogenic topography in southern Africa. Geology. 41(3), 331-334.
686 https://doi.org/10.1130/G33806.1.
687 Schwanghart, W., Scherler, D., 2014. Short communication: TopoToolbox 2 – MATLAB-
688 based software for topographic analysis and modeling in Earth surface sciences. Earth
689 Surf. Dyn.2, 1–7. https://doi.org/10.5194/esurf-2-1-2014.
690 Sébrier, M., Siame, L., Zouine, E. M., Winter, T., Missenard, Y., Leturmy, P., 2006. Active
691 tectonics in the moroccan high atlas. C.R. Geosci. 338(1-2), 65-79.
692 https://doi.org/10.1016/j.crte.2005.12.001.
693 Seybold, H., Berghuijs, W. R., Prancevic, J. P., & Kirchner, J. W., 2021. Global dominance
694 of tectonics over climate in shaping river longitudinal profiles. Nat. Geosci. 14(7),
695 503-507. https://doi.org/10.1038/s41561-021-00810-4.

696 Snyder, N. P., Whipple, K. X., Tucker, G. E., Merritts, D. J., 2003. Importance of a stochastic
697 distribution of floods and erosion thresholds in the bedrock river incision problem. J.
698 Geophys. Res., Solid Earth. 108(B2). https://doi.org/10.1029/2001JB001655.
699 Soulaimani, A., Michard, A., Ouanaimi, H., Baidder, L., Raddi, Y., Saddiqi, O., Rjimati, E.
700 C., 2014. Late Ediacaran–Cambrian structures and their reactivation during the
701 Variscan and Alpine cycles in the Anti-Atlas (Morocco). J. Afr. Earth. Sci. 98, 94-112.
702 https://doi.org/10.1016/j.jafrearsci.2014.04.025.
703 Stock, J. D., Montgomery, D. R., 1999. Geologic constraints on bedrock river incision using
704 the stream power law. J. Geophys. Res., Solid Earth. 104(B3), 4983-4993.
705 https://doi.org/10.1029/98JB02139.
706 von Blanckenburg, F., 2005. The control mechanisms of erosion and weathering at basin
707 scale from cosmogenic nuclides in river sediment. Earth and Planet. Sci. Lett. 237(3-
708 4), 462-479. https://doi.org/10.1016/j.epsl.2005.06.030.
709 Whipple, K.X., Tucker, G.E., 1999. Dynamics of the stream-power river incision model:
710 implications for height limits of mountain ranges, landscape response timescales, and
711 research needs. J. Geophys. Res., Solid Earth. 104, 17661–17674.
712 https://doi.org/10.1029/1999JB900120.
713 Willett, S. D., Brandon, M. T., 2002. On steady states in mountain belts. Geology. 30(2),
714 175-178. https://doi.org/10.1130/0091-7613(2002)030<0175:OSSIMB>2.0.CO;2.
715 Zhang, Z., Ramstein, G., Schuster, M., Li, C., Contoux, C., Yan, Q., 2014. Aridification of
716 the Sahara desert caused by Tethys Sea shrinkage during the Late
717 Miocene. Nature. 513(7518), 401-404. https://doi.org/10.1038/nature13705.
718 Zondervan, J. R., Stokes, M., Boulton, S. J., Telfer, M. W., Mather, A. E., 2020. Rock
719 strength and structural controls on fluvial erodibility: Implications for drainage divide

720 mobility in a collisional mountain belt. Earth and Planet. Sci. Lett. 538, 116221.
721 https://doi.org/10.1016/j.epsl.2020.116221.

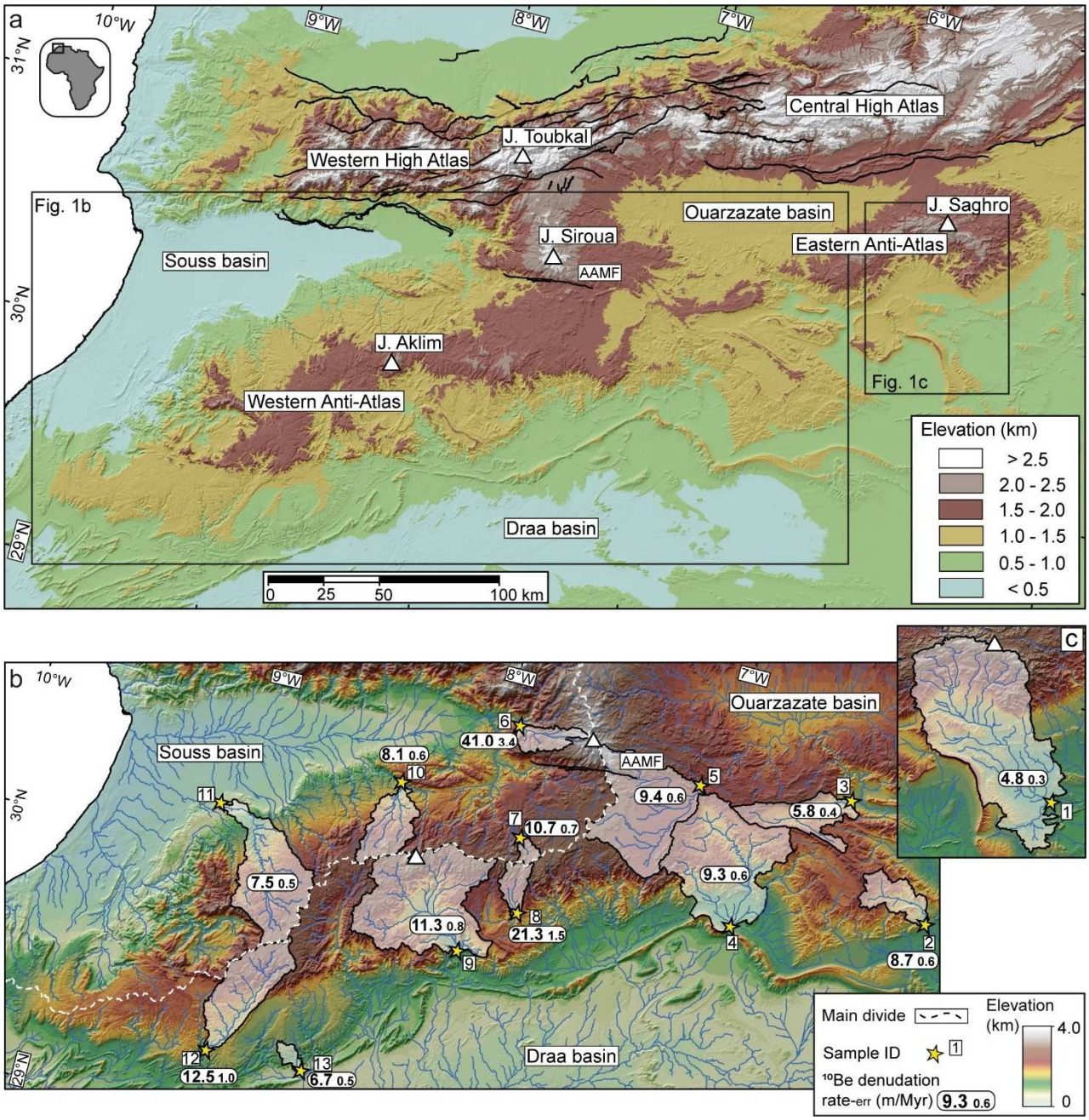

Figure 1. a) Digital elevation model of the High Atlas and the Anti-Atlas Mountains (SRTM DEM, pixel size 90 m). The black lines are the major tectonic lineaments. **b-c)** Topographic map of the Anti-Atlas and the Siroua Massif, with ^{10}Be sampling locations. The white polygons are the limits of the sampled catchments. The sample ID is used in Table S1 of the supplementary material. AAMF: Anti-Atlas Major Fault.

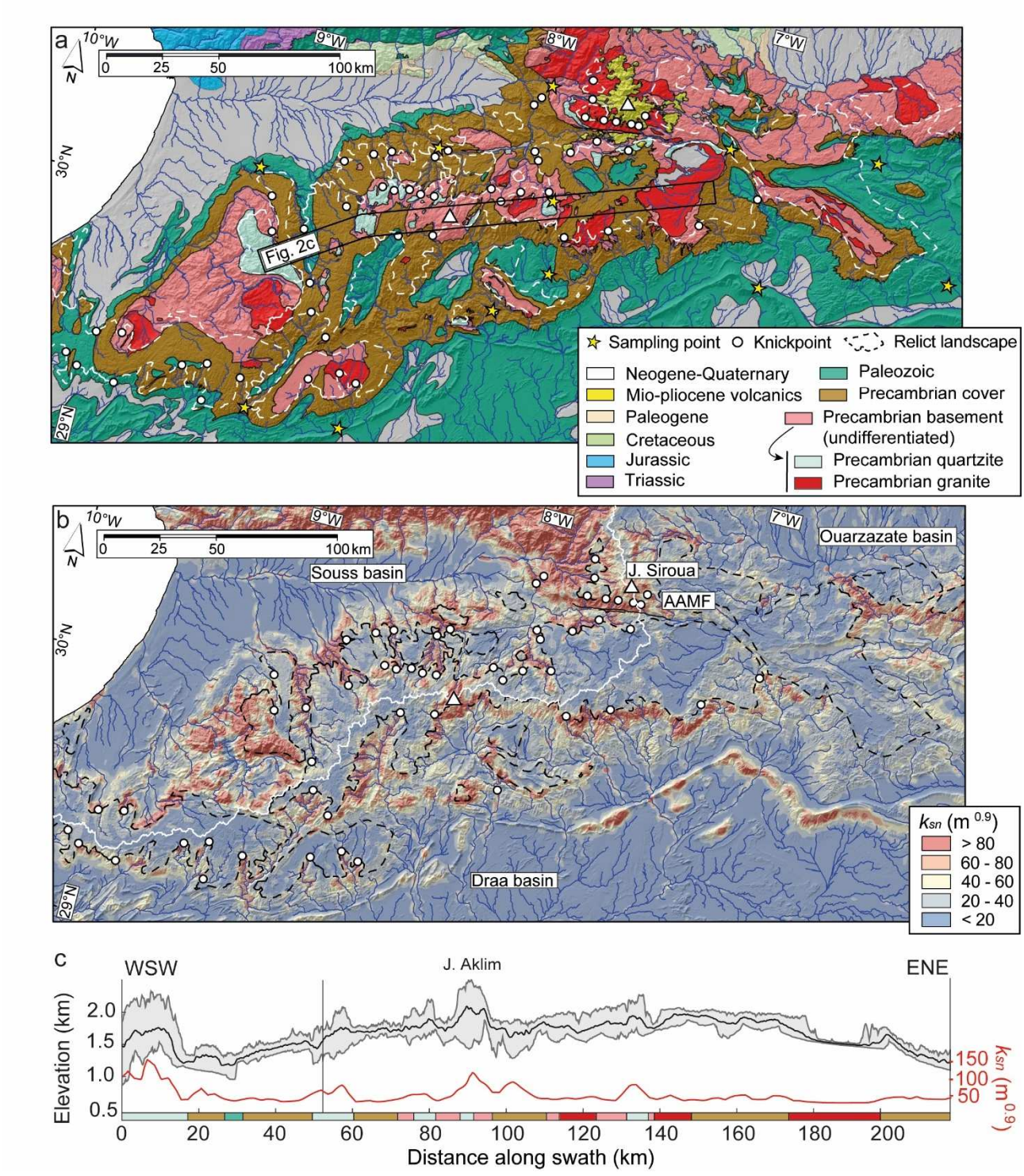

Figure 2. a) Geological map of the Anti-Atlas and the Siroua Massif (after Hollard et al., 1985) and **b)** interpolated map of k_{sn} values. The white line and triangle indicate the main drainage divide and topographic peaks, respectively. **c)** Topographic swath profile along the main divide of the Anti-Atlas Mountains (location in figure 2a).

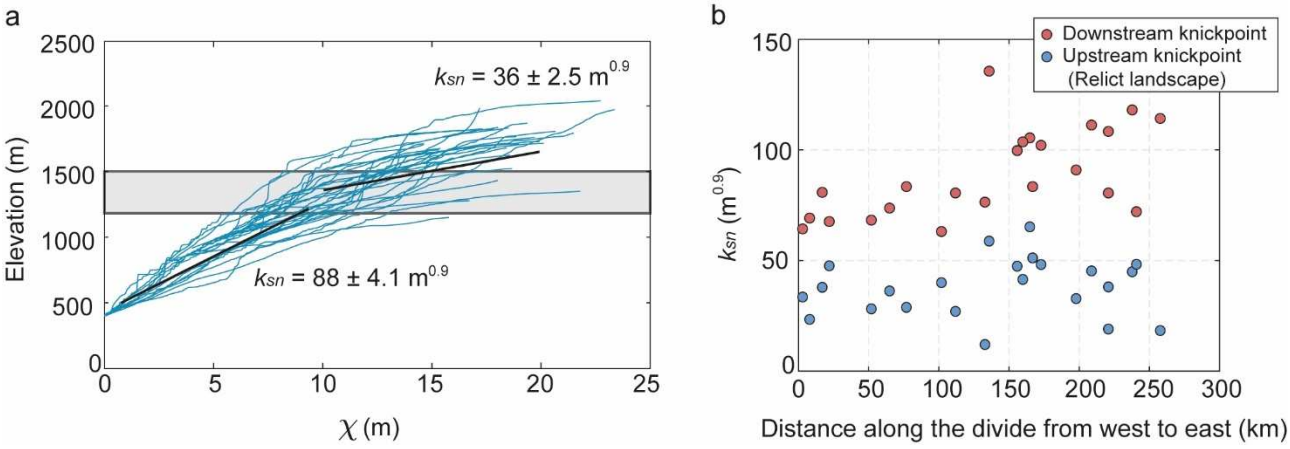

Figure 3. a) χ- transformed profiles of the main streams draining the central Anti-Atlas. All rivers are extracted from the bedrock-alluvial transition, which is at about 400 m. The non-lithological knickpoints are located between 1200 and 1500 m (grey band) and separate segments with different k_{sn} value (see Table S2 for details). The numbers in the plot represent the mean k_{sn} and associated standard error upstream and downstream the grey band. **b)** k_{sn} values upstream and downstream of major non-lithological knickpoints from the main river trunks.

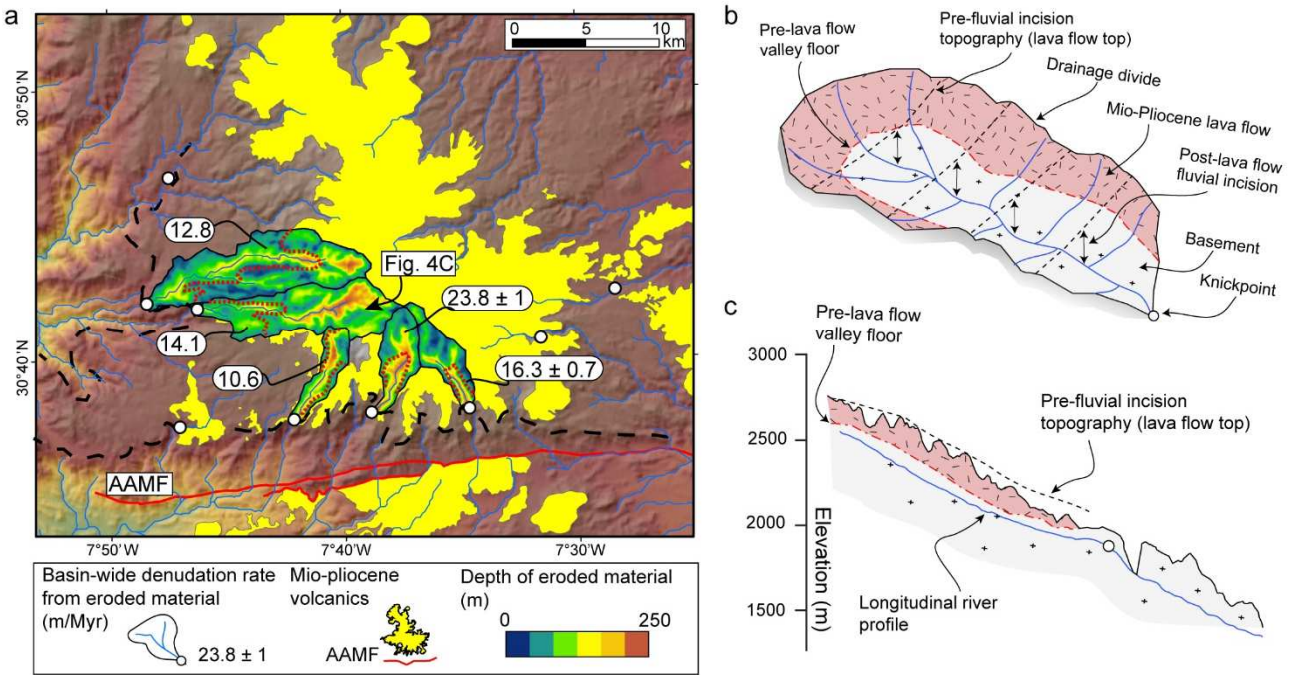

Figure 4. a) Digital elevation model of the Siroua Massif with the depth of eroded rock volumes and resulting denudation rates (see Table S3). The dashed black line and the white circles demark the uplifted relict landscape and non-lithological knickpoints, respectively. The dashed red lines within the basins represent the lava-basement contact. **b)** Schematic 3D sketch of the Siroua landscape. The eroded rock volume is calculated from the highest point of the lava flows upstream of non-lithological knickpoints. Based on the age of the lavas, the eroded volumes are translated into denudation rates (see methods for details). **c)** Simplified geological cross section and river profile of a selected catchment.

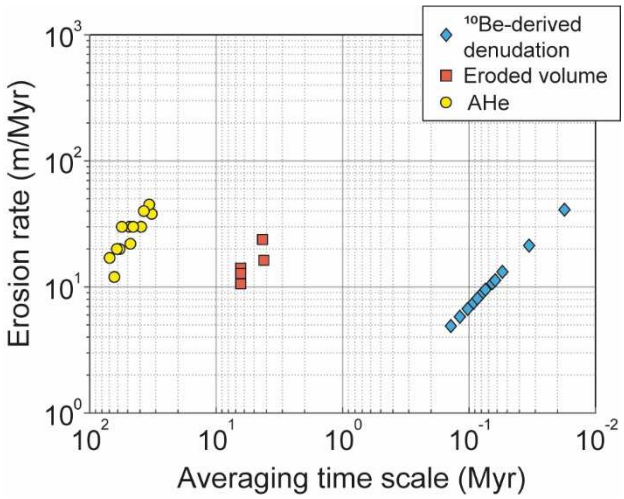

Figure 5. Erosion rates for the Anti-Atlas and the Siroua Massif for different time scales. Long-term erosion rates (AHe) are from thermochronologic ages (Lanari et al., 2020a) and eroded volumes of Mio-Pliocene volcanics exposed in the Siroua Massif (this study; see Table S3 for details). Short-term denudation rates are from ^{10}Be data (this study; see Table S1 for details).

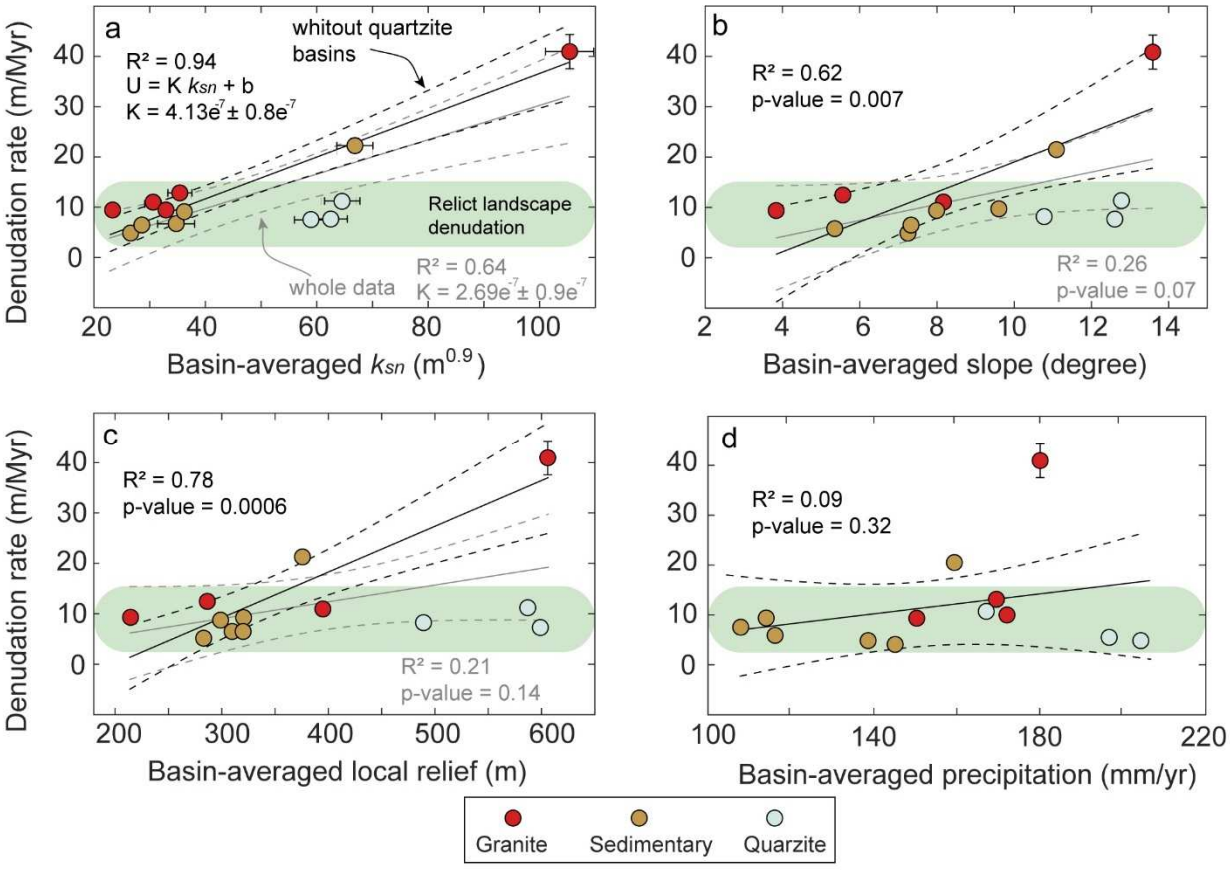

Figure 6. Basin-wide denudation rate vs basin-averaged **a)** k_{sn}, **b)** slope, **c)** local relief (2.5 km radius), and **d)** precipitation rate for different rock types exposed in the sampled basins. The solid line represents the linear best-fit, while the dashed black line delimits the bootstrapped 95% confidence interval considering only basins composed of granite and sedimentary rocks. The grey line denotes the best-fit considering all sampled basins, while the dashed grey line is the associated bootstrapped 95% confidence interval.

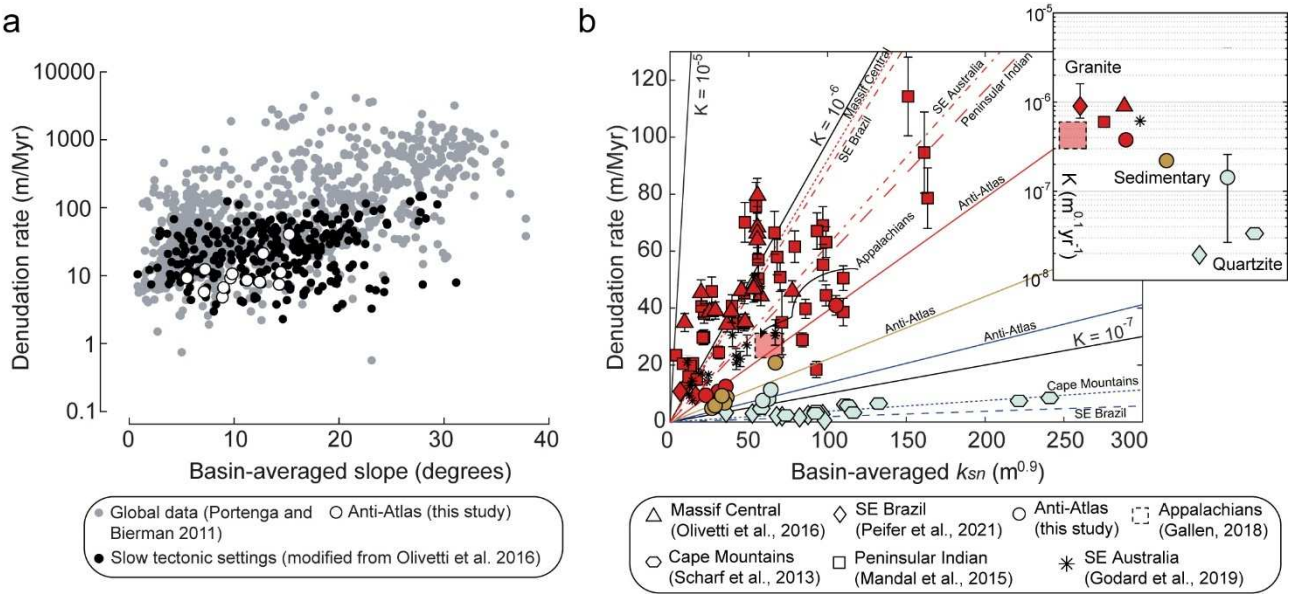

Figure 7. a) Global compilation of slope versus basin-wide denudation rate. **b)** Comparison of basin-averaged k_{sn} value versus denudation rate for different rock-types (red: granitic rocks, brown: sedimentary rocks, light blue: quartzite) in slow tectonic settings. The solid lines show the forced linear best-fit (see Table S6 for details).

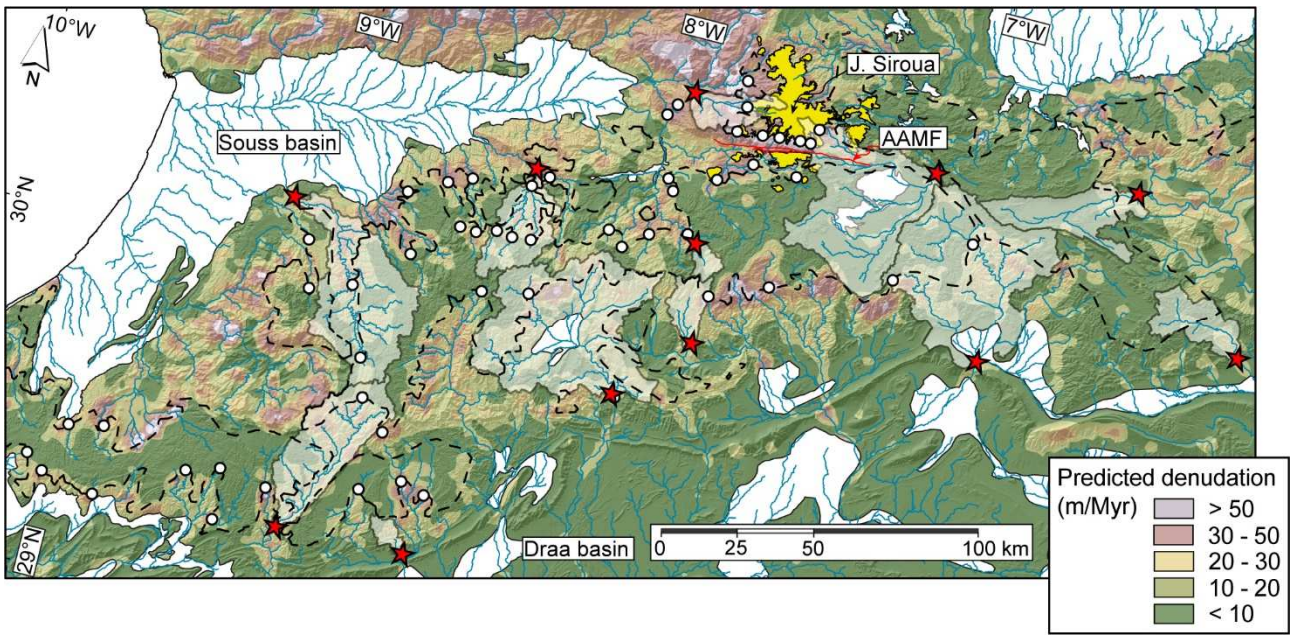

Figure 8. Predicted denudation rates based on the distribution of normalized channel steepness (k_{sn}), using different erodibility values for each lithology and n =1. Red stars and whitish polygons are sampling sites and relative catchments, respectively.

Lithological control on topographic relief evolution in a slow tectonic setting (Anti-Atlas, Morocco)

Methods

a) ^{10}Be-derived denudation rates

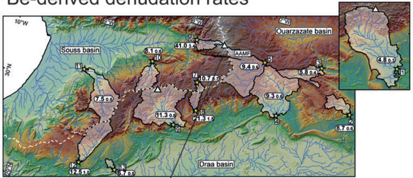

b) Erosion rates from incised lava flows

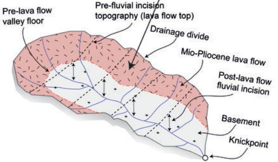

c) Global compilation

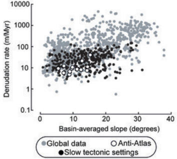

Results

a) Erosional steady-state of the relict landscape

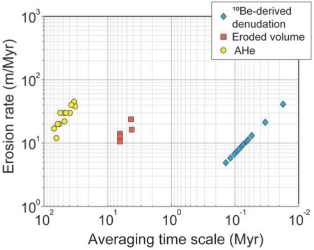

b) Lithological control on topography and quantification of *K*